Investigation of intense sheet electron beam transport using the macroscopic cold-fluid model and the single-particle orbit theory*

Han Ying(韩 莹)[a)b)†] and Ruan Cun-Jun(阮存军)[a)]

[a)] *Key Laboratory of High Power Microwave Sources and Technologies, Institute of Electronics, Chinese Academy of Sciences, Beijing* 100190, *China*

[b)] *Graduate University of Chinese Academy of Sciences, Beijing* 100039, *China*

(Received 28 April 2011; revised manuscript received 8 December 2011)

The focusing and the stable transport of an intense elliptic sheet electron beam in a uniform magnetic field are investigated thoroughly by using the macroscopic cold-fluid model and the single-particle orbit theory. The results indicate that the envelopes and the tilted angles of the sheet electron beam obtained by the two theories are consistent. The single-particle orbit theory is more accurate due to its treatment of the space-charge fields in a rectangular drift tube. The macroscopic cold-fluid model describes the collective transport process in order to provide detailed information about the beam dynamics, such as beam shape, density, and velocity profile. The tilt of the elliptic sheet beam in a uniform magnetic field is carefully studied and demonstrated. The results presented in this paper provide two complete theories for systemically discussing the transport of the sheet beam and are useful for understanding and guiding the practical engineering design of electron optics systems in high power vacuum electronic devices.

Keywords: focusing and transport, macroscopic cold-fluid model, sheet electron beam, single-particle orbit theory

PACS: 41.75.–i, 41.85.–p, 41.85.Ja, 41.90.+e **DOI:** 10.1088/1674-1056/21/5/054103

1. Introduction

Intense sheet electron beams have received much attention in recent years due to their numerous applications, such as high power microwave sources and advanced accelerators. The sheet beam has a large aspect ratio, so it can have a very high current with a small current density. This prominent characteristic can be used in high power and high frequency applications. The key challenges to realizing sheet beam devices are the focusing and the stable transport of the sheet beam, which have been studied for several decades.

As is well known, a sheet beam is unstable when propagating through a uniform magnetic field due to the $\boldsymbol{E} \times \boldsymbol{B}$ velocity shear effect. Diocotron instability results in beam kinks, vortices, and eventual filamentation,[1,2] which are the key indicators that a uniform magnetic field may not be used to focus sheet beams. In order to avoid diocotron instability, periodic focusing fields, including periodic cusped magnetic (PCM) fields and wiggler magnetic fields, were proposed and analysed in detail according to the classical work of Booske *et al.*[3,4] The periodic magnetic fields effectively implement the focusing and the stable transport of the sheet beams.[5,6] In recent years, the periodic focusing configurations have received much attention for practical applications. Using a uniform magnetic field as a focusing method has many characteristic advantages in comparison with the PCM and the wiggler fields, such as simple configuration, low cost, and achievable higher field. In order to focus the sheet beam in both transverse planes, the improved periodic configurations, including the offset-pole Wiggler, the offset-pole PCM, and the PCM-PQM (periodic quadrupole magnet) structures,[7] are usually employed. Thus, the actual periodic magnetic configurations are even more complex and prone to magnetic field errors due to the mechanical misalignments, which of course enhances the difficulty in manufacture. In particular, the periodic focusing introduces a cutoff voltage that arises from the single-particle orbit stability.[8] The physical limitation has become a key impediment to the advancement of vacuum elec-

*Project supported by the National Natural Science Foundation of China (Grant Nos. 60501019, 10775139 and 60971073).

†Corresponding author. E-mail: helen_han@139.com

© 2012 Chinese Physical Society and IOP Publishing Ltd

tron devices based on a high current density and a low voltage sheet beam. Therefore, when we designed a W-band sheet beam klystron, the solenoid configuration is chosen to provide a uniform magnetic field for focusing an elliptic sheet beam. A sample tube has been built and tested successfully. The transmission efficiency reaches up to over 98% at voltages ranging from 20 kV to 80 kV.

In general, for the space-charge-dominated sheet electron beam in the limit of negligibly small thermal emittance, the single-particle orbit theory is used widely for investigating the beam transport theoretically,[8,9] which can give the trajectories of the electrons projected at arbitrary initial positions. However, this analysis cannot describe the collective transport process. In this paper, a macroscopic cold-fluid model is used to study the focusing and the transport of an elliptic sheet electron beam as a collective beam in uniform magnetic fields, which gives detailed information about the beam dynamics, such as beam shape, density, and velocity profile. A comparison between the two theories indicates that the results accord very well with each other and the single-particle orbit theory is more accurate due to treating the space-charge fields in the rectangular drift tube. It is interesting to note that the elliptic sheet beam is tilted during its transport in a uniform magnetic field, as demonstrated in the investigation.

2. Macroscopic cold-fluid model theory

We consider a space-charge dominated elliptic intense beam propagating in the direction parallel to an axial magnetic field $B_0\boldsymbol{e}_z$ with a velocity of $v_\mathrm{b}\boldsymbol{e}_z$, where $\boldsymbol{e}_z$ is a unit vector along the z axis. The emittance effect is negligibly small, so the beam can be described by the macroscopic cold-fluid model. In the paraxial approximation, the equations for time-stationary flow ($\partial/\partial t = 0$) are[10,11]

$$\beta_\mathrm{b} c\frac{\partial n_\mathrm{b}}{\partial z} + \boldsymbol{\nabla}_\perp \cdot (n_\mathrm{b}\boldsymbol{v}_\perp) = 0, \tag{1}$$

$$\boldsymbol{\nabla}_\perp^2 \phi = c\beta_\mathrm{b}^{-1}\boldsymbol{\nabla}_\perp^2 A_z = en_\mathrm{b}/\varepsilon_0, \tag{2}$$

$$n_\mathrm{b}\left(\beta_\mathrm{b} c\frac{\partial}{\partial z} + \boldsymbol{v}_\perp \cdot \boldsymbol{\nabla}_\perp\right)\boldsymbol{v}_\perp = -\frac{en_\mathrm{b}}{\gamma_\mathrm{b} m_0}\left(-\gamma_\mathrm{b}^{-2}\boldsymbol{\nabla}_\perp\varphi + \boldsymbol{v}_\perp \times B_0\boldsymbol{e}_z\right), \tag{3}$$

where $\boldsymbol{\nabla}_\perp = \partial/\partial\boldsymbol{x}_\perp$, $\boldsymbol{x}_\perp = x\boldsymbol{e}_x + y\boldsymbol{e}_y$, $\boldsymbol{v}_\perp$ and n_b are the electron transverse velocity and the electron density of the electron fluid element, respectively, $\beta_\mathrm{b} = v_\mathrm{b}/c \approx$ const, $\gamma_\mathrm{b} = \left(1 - \beta_\mathrm{b}^2/c^2\right)^{-1/2}$ is the relativistic mass factor, c is the velocity of light in vacuum, $-e$ and m_0 are the electron charge and the electron rest mass, respectively, ϕ is the space-charge scalar electric potential, and A_z is the vector self-magnetic potential in the z direction. It is necessary to note that we have implicitly incorporated self-magnetic fields through a γ_b^{-2} reduction of the space-charge fields in Eq. (3).

The elliptic sheet beam propagating through a uniform magnetic field will be tilted due to the adverse effects at the two sides along the x axis, as illustrated in Fig. 1, which shows the laboratory and the tilted coordinate systems. Here, $\boldsymbol{x} = x\boldsymbol{e}_x + y\boldsymbol{e}_y + z\boldsymbol{e}_z$ is the displacement in the laboratory coordinate system, $\tilde{\boldsymbol{x}} = \tilde{x}\boldsymbol{e}_{\tilde{x}} + \tilde{y}\boldsymbol{e}_{\tilde{y}} + s\boldsymbol{e}_s$ is the displacement in the tilted coordinate system, and $\theta(s)$ is the tilted angle of the ellipse. It is easy to acquire the relationships $\tilde{x}' = \tilde{y}\theta'$, $\tilde{y}' = -\tilde{x}\theta'$, $\partial\boldsymbol{e}_{\tilde{x}}/\partial s = \theta'\boldsymbol{e}_{\tilde{y}}$, and $\partial\boldsymbol{e}_{\tilde{y}}/\partial s = -\theta'\boldsymbol{e}_{\tilde{x}}$, where the prime denotes $\partial/\partial s$.

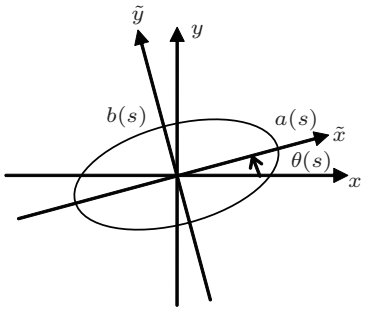


Fig. 1. Laboratory and tilted coordinate systems.

Assuming that the electron density per unit length is unchangeable, the beam keeps an elliptic form, and the density profile is uniform, we obtain the solutions for Eqs. (1)–(3) as

$$n_\mathrm{b}(\tilde{\boldsymbol{x}}_\perp, s) = \frac{N_\mathrm{b}}{\pi a(s) b(s)}\Theta\left[1 - \frac{\tilde{x}^2}{a^2(s)} - \frac{\tilde{y}^2}{b^2(s)}\right], \tag{4}$$

and

$$\boldsymbol{v}_\perp(\tilde{\boldsymbol{x}}_\perp, s) = [\mu_x(s)\tilde{x} - \alpha_x(s)\tilde{y}]\beta_\mathrm{b} c\boldsymbol{e}_{\tilde{x}} + [\mu_y(s)\tilde{y} + \alpha_y(s)\tilde{x}]\beta_\mathrm{b} c\boldsymbol{e}_{\tilde{y}}, \tag{5}$$

where $\tilde{\boldsymbol{x}}_\perp = \tilde{x}\boldsymbol{e}_{\tilde{x}} + \tilde{y}\boldsymbol{e}_{\tilde{y}}$ is the transverse displacement in the tilted coordinate system, N_b is the electron density per unit length, $\Theta(x)$ is the step function, $\Theta(x) = 1$ if $x > 0$, $\Theta(x) = 1/2$ if $x = 0$, and $\Theta(x) = 0$ if $x < 0$.

As is well known, the space-charge electric potential for an elliptic beam with the density distribution specified in Eq. (4) can be expressed as

$$\phi = \frac{eN_{\rm b}}{2\varepsilon_0\pi\,(a+b)}\left(\frac{\tilde{x}^2}{a}+\frac{\tilde{y}^2}{b}\right). \tag{6}$$

Substituting Eqs. (4)–(6) into Eq. (1), we obtain the following equation:

$$\begin{aligned}&\left(-\frac{b'}{ab^2}-\frac{a'}{a^2b}\right)\Theta\left(1-\frac{\tilde{x}^2}{a^2}-\frac{\tilde{y}^2}{b^2}\right)\\&+2\left[\left(\frac{a'}{a}-\mu_x\right)\frac{\tilde{x}^2}{a^2}+\left(\frac{b'}{b}-\mu_y\right)\frac{\tilde{y}^2}{b^2}\right.\\&\left.+\left(-\frac{b}{a}\theta'+\frac{a}{b}\theta'+\frac{b}{a}\alpha_x-\frac{a}{b}\alpha_y\right)\frac{\tilde{x}\tilde{y}}{ab}\right]\\&\times\delta\left(1-\frac{\tilde{x}^2}{a^2}-\frac{\tilde{y}^2}{b^2}\right)=0,\end{aligned} \tag{7}$$

where $\delta(x)$ is the delta function. Only when the coefficients of terms Θ, $\tilde{x}^2\delta$, $\tilde{y}^2\delta$, and $\tilde{x}\tilde{y}\delta$ all equal to zero, will Eq. (7) will be satisfied for arbitrary $\tilde{x}$ and $\tilde{y}$. Thus, the following equations are obtained:

$$\mu_x = a'/a, \tag{8}$$

$$\mu_y = b'/b, \tag{9}$$

$$\theta' = \left(a^2\alpha_y - b^2\alpha_x\right)/\left(a^2-b^2\right). \tag{10}$$

Substituting Eqs. (5) and (6) into Eq. (3) and using the relations $\partial\boldsymbol{e}_{\tilde{x}}/\partial s = \theta'\boldsymbol{e}_{\tilde{y}}$ and $\partial\boldsymbol{e}_{\tilde{y}}/\partial s = -\theta'\boldsymbol{e}_{\tilde{x}}$, we can obtain the two equations in the $\tilde{x}$ and the $\tilde{y}$ directions respectively as

$$\begin{aligned}&\beta_{\rm b}c\frac{\partial}{\partial s}\left[\beta_{\rm b}c\left(\mu_x\tilde{x}-\alpha_x\tilde{y}\right)\right]-\beta_{\rm b}c\theta'\beta_{\rm b}c\left(\mu_y\tilde{y}+\alpha_y\tilde{x}\right)\\&+\beta_{\rm b}c\left(\mu_x\tilde{x}-\alpha_x\tilde{y}\right)\frac{\partial}{\partial\tilde{x}}\left[\beta_{\rm b}c\left(\mu_x\tilde{x}-\alpha_x\tilde{y}\right)\right]\\&+\beta_{\rm b}c\left(\mu_y\tilde{y}+\alpha_y\tilde{x}\right)\frac{\partial}{\partial\tilde{y}}\left[\beta_{\rm b}c\left(\mu_x\tilde{x}-\alpha_x\tilde{y}\right)\right]\\=&-\frac{e}{\gamma_{\rm b}m_0}\left[-\frac{eN_{\rm b}\tilde{x}}{\gamma_{\rm b}^2\varepsilon_0\pi\,(a+b)\,a}\right.\\&\left.+\beta_{\rm b}c\left(\mu_y\tilde{y}+\alpha_y\tilde{x}\right)B_0\right],\end{aligned} \tag{11}$$

$$\begin{aligned}&\beta_{\rm b}c\frac{\partial}{\partial s}\left[\beta_{\rm b}c\left(\mu_y\tilde{y}+\alpha_y\tilde{x}\right)\right]+\beta_{\rm b}c\theta'\beta_{\rm b}c\left(\mu_x\tilde{x}-\alpha_x\tilde{y}\right)\\&+\beta_{\rm b}c\left(\mu_x\tilde{x}-\alpha_x\tilde{y}\right)\frac{\partial}{\partial\tilde{x}}\left[\beta_{\rm b}c\left(\mu_y\tilde{y}+\alpha_y\tilde{x}\right)\right]\\&+\beta_{\rm b}c\left(\mu_y\tilde{y}+\alpha_y\tilde{x}\right)\frac{\partial}{\partial\tilde{y}}\left[\beta_{\rm b}c\left(\mu_y\tilde{y}+\alpha_y\tilde{x}\right)\right]\\=&-\frac{e}{\gamma_{\rm b}m_0}\left[-\frac{eN_{\rm b}\tilde{y}}{\gamma_{\rm b}^2\varepsilon_0\pi\,(a+b)\,b}\right.\\&\left.-\beta_{\rm b}c\left(\mu_x\tilde{x}-\alpha_x\tilde{y}\right)B_0\right].\end{aligned} \tag{12}$$

Equations (11) and (12) can be simplified into

$$f_x\tilde{x}+g_y\tilde{y}=0 \tag{13}$$

and

$$g_x\tilde{x}+f_y\tilde{y}=0, \tag{14}$$

respectively, where

$$\begin{aligned}f_x =\;&\mu_x^2+\mu_x'-\alpha_x\alpha_y+\left(\alpha_x-\alpha_y\right)\theta'\\&-\frac{e^2N_{\rm b}}{\gamma_{\rm b}^3m_0\beta_{\rm b}^2c^2\varepsilon_0\pi a\,(a+b)}+\frac{eB_0}{\gamma_{\rm b}m_0\beta_{\rm b}c}\alpha_y,\end{aligned} \tag{15}$$

$$\begin{aligned}f_y =\;&\mu_y^2+\mu_y'-\alpha_x\alpha_y-\left(\alpha_x-\alpha_y\right)\theta'\\&-\frac{e^2N_{\rm b}}{\gamma_{\rm b}^3m_0\beta_{\rm b}^2c^2\varepsilon_0\pi b\,(a+b)}+\frac{eB_0}{\gamma_{\rm b}m_0\beta_{\rm b}c}\alpha_x,\end{aligned} \tag{16}$$

$$\begin{aligned}g_x =\;&\alpha_y'+\left(\mu_x-\mu_y\right)\theta'+\left(\mu_x+\mu_y\right)\alpha_y\\&-\frac{eB_0}{\gamma_{\rm b}m_0\beta_{\rm b}c}\mu_x,\end{aligned} \tag{17}$$

$$\begin{aligned}g_y =\;&-\alpha_x'+\left(\mu_x-\mu_y\right)\theta'-\left(\mu_x+\mu_y\right)\alpha_x\\&+\frac{eB_0}{\gamma_{\rm b}m_0\beta_{\rm b}c}\mu_y.\end{aligned} \tag{18}$$

Likewise, coefficients f_x, f_y, g_x, and g_y of $\tilde{x}$ and $\tilde{y}$ in Eqs. (13) and (14) must be identical to zero simultaneously to make Eqs. (13) and (14) hold. Using Eqs. (8)–(10), we can obtain the following beam envelope equations from Eqs. (15)–(18):

$$\begin{aligned}&\frac{{\rm d}^2a}{{\rm d}s^2}-\left[\frac{b^2\left(\alpha_x^2-2\alpha_x\alpha_y\right)+a^2\alpha_y^2}{a^2-b^2}-\frac{eB_0\alpha_y}{\gamma_{\rm b}m_0\beta_{\rm b}c}\right]a\\&-\frac{e^2N_{\rm b}}{\gamma_{\rm b}^3m_0\beta_{\rm b}^2c^2\varepsilon_0\pi\,(a+b)}=0,\end{aligned} \tag{19}$$

$$\begin{aligned}&\frac{{\rm d}^2b}{{\rm d}s^2}+\left[\frac{a^2\left(\alpha_y^2-2\alpha_x\alpha_y\right)+b^2\alpha_x^2}{a^2-b^2}-\frac{eB_0\alpha_x}{\gamma_{\rm b}m_0\beta_{\rm b}c}\right]b\\&-\frac{e^2N_{\rm b}}{\gamma_{\rm b}^3m_0\beta_{\rm b}^2c^2\varepsilon_0\pi\,(a+b)}=0,\end{aligned} \tag{20}$$

$$\begin{aligned}&\frac{\rm d}{{\rm d}s}\left(a^2\alpha_y\right)-\frac{ab^3\left(\alpha_x-\alpha_y\right)}{a^2-b^2}\frac{\rm d}{{\rm d}s}\left(\frac{a}{b}\right)\\&-\frac{eB_0}{\gamma_{\rm b}m_0\beta_{\rm b}c}a\frac{{\rm d}a}{{\rm d}s}=0,\end{aligned} \tag{21}$$

$$\begin{aligned}&\frac{\rm d}{{\rm d}s}\left(b^2\alpha_x\right)-\frac{a^3b\left(\alpha_x-\alpha_y\right)}{a^2-b^2}\frac{\rm d}{{\rm d}s}\left(\frac{b}{a}\right)\\&-\frac{eB_0}{\gamma_{\rm b}m_0\beta_{\rm b}c}b\frac{{\rm d}b}{{\rm d}s}=0.\end{aligned} \tag{22}$$

3. Single-particle orbit theory

As indicated by the model built in Section 2, in the paraxial approximation, the relativistic electron envelope equations of motion are

$$x'' = -\frac{e}{\gamma_{\rm b}^3m_0v_{\rm b}^2}E_x-\frac{eB_0}{\gamma_{\rm b}m_0v_{\rm b}}y' \tag{23}$$

and

$$y'' = -\frac{e}{\gamma_{\rm b}^3 m_0 v_{\rm b}^2} E_y + \frac{eB_0}{\gamma_{\rm b} m_0 v_{\rm b}} x'. \tag{24}$$

By calculating the space-charge fields, we can obtain the trajectories of electrons injected in the direction parallel to the z axis at arbitrary initial positions.[11] For a long elliptic sheet beam propagating in a rectangular drift tube, the electric potential distribution and the space-charge fields are independent of the axial direction, and they can be obtained by numerical calculation in the transverse section.[3] We assume that the width of the drift tube is w in the x direction and the height is h in the y direction, the semi-major and the semi-minor axes of the elliptic sheet beam are a and b, respectively. For the beam with a uniform density profile, the space-charge fields can be expressed as

$$E_x = \begin{cases} -\dfrac{2en_{\rm b}}{\pi\varepsilon_0} \displaystyle\sum_{m=0}^{\infty} \dfrac{\cos\left[(2m+1)\,\pi y/h\right]}{2m+1} C_1\,(a), & a < x < w/2, \\ -\dfrac{2en_{\rm b}}{\pi\varepsilon_0} \displaystyle\sum_{m=0}^{\infty} \dfrac{\cos\left[(2m+1)\,\pi y/h\right]}{2m+1} \left[C_1\,(x) - C_2\,(x)\right], & -a \le x \le a, \\ \dfrac{2en_{\rm b}}{\pi\varepsilon_0} \displaystyle\sum_{m=0}^{\infty} \dfrac{\cos\left[(2m+1)\,\pi y/h\right]}{2m+1} C_2\,(-a), & -w/2 < x < -a, \end{cases} \tag{25}$$

and

$$E_y = \begin{cases} -\dfrac{2en_{\rm b}}{\pi\varepsilon_0} \displaystyle\sum_{m=0}^{\infty} \dfrac{\sin\left[(2m+1)\,\pi y/h\right]}{2m+1} C_1\,(a)\,, & a < x < w/2, \\ -\dfrac{2en_{\rm b}}{\pi\varepsilon_0} \displaystyle\sum_{m=0}^{\infty} \dfrac{\sin\left[(2m+1)\,\pi y/h\right]}{2m+1} \left[C_1\,(x) + C_2\,(x)\right], & -a \le x \le a, \\ -\dfrac{2en_{\rm b}}{\pi\varepsilon_0} \displaystyle\sum_{m=0}^{\infty} \dfrac{\sin\left[(2m+1)\,\pi y/h\right]}{2m+1} C_2\,(-a)\,, & -w/2 < x < -a, \end{cases} \tag{26}$$

where

$$C_1 = \int_{-a}^{x} {\rm d}x' \sin\left[(2m+1)\,\pi b\sqrt{1 - x'^2/a^2}/h\right] \times {\rm e}^{-\frac{(2m+1)\pi(x-x')}{h}}, \tag{27}$$

$$C_2 = \int_{x}^{a} {\rm d}x' \sin\left[(2m+1)\,\pi b\sqrt{1 - x'^2/a^2}/h\right] \times {\rm e}^{-\frac{(2m+1)\pi(x'-x)}{h}}. \tag{28}$$

The variations of normalized space-charge fields $E_{x_\rm norm}$ with x in the $y = 0$ plane and $E_{y_\rm norm}$ with y in the $x = 0$ plane for the elliptic sheet electron beam in a drift tube are plotted in Figs. 2(a) and 2(b), respectively. The structural parameters used are $w = 15$ mm, $h = 1$ mm, $a = 5$ mm, $b = 0.25$ mm, voltage $V_0 = 80$ kV, and current $I_0 = 4.07$ A. The solid lines in Figs. 2(a) and 2(b) represent the normalized space-charge fields $E_{x_\rm norm}$ and $E_{y_\rm norm}$ for the inside of the elliptic electron beam in free space, respectively. The curves in Figs. 2(a) and 2(b) are normalized to the maximum values of E_x and E_y in the drift tube, respectively. It is found that $E_{x_\rm norm}$ of the elliptic beam in the drift tube is much smaller than that in free space and $E_{y_\rm norm}$ of the elliptic beam in the drift tube is little larger than that in free space due to the effect of conducting walls. Therefore, it is expected that the oscillation amplitude of envelope in the x direction calculated with the macroscopic cold-fluid model is much larger, while it is somewhat smaller in the y direction, which will be shown later.

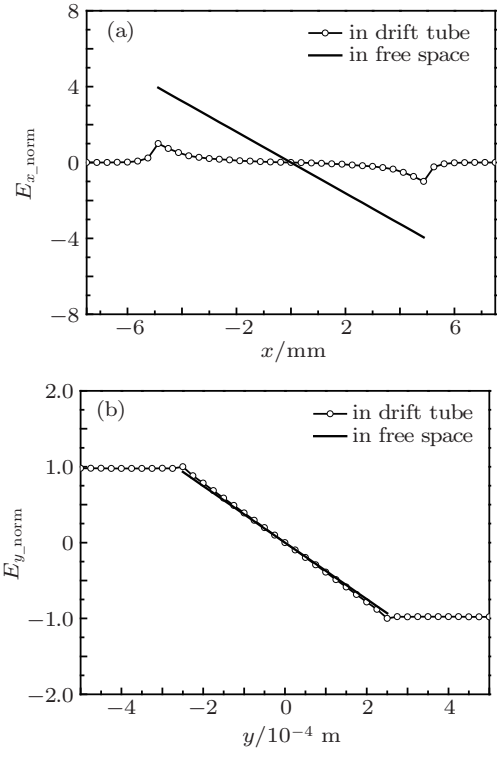


Fig. 2. (a) Variations of normalized space-charge fields $E_{x_\rm norm}$ with x in the $y = 0$ plane and (b) $E_{y_\rm norm}$ with y in the $x = 0$ plane.

4. Examples

The numerical calculations are used to investigate the transport of an elliptic sheet electron beam in a uniform magnetic field based on the macroscopic cold-fluid model and the single-particle orbit theory described in Sections 2 and 3. As an example, we consider an elliptic sheet electron beam designed with voltages V_0 ranging from 20 kV to 80 kV and perveance $P_{\rm er} = 0.18$ μP, thus current I_0 is in the range from 0.51 A to 4.07 A. The approximately uniform magnetic field distribution is shown in Fig. 3. The distance of transport is $l = 100$ mm.

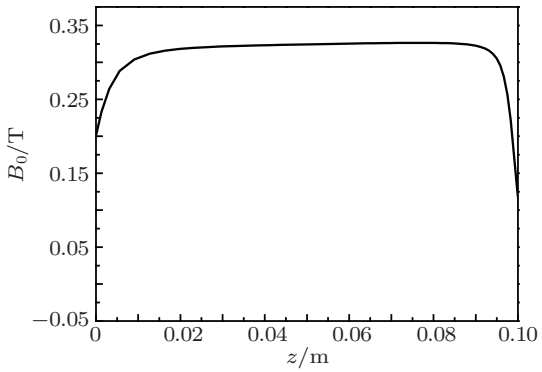


Fig. 3. Approximately uniform magnetic field distribution along the z axis.

The solutions of envelope Eqs. (19)–(22) are calculated numerically with different voltages and currents. Figure 4(a)–4(c) show envelopes $a\,(s)$, $b\,(s)$ and values of tilted angle $\theta\,(s)$ for various voltages and currents, respectively. It is concluded that stable transport with small envelope oscillations are realized in the tilted coordinate system and the tilted angle has an oscillatory augmentation. The amplitude and the period length of oscillation and the tilted angle increase as the current increases. For the transport distance of 100 mm, the tilted angle is only about 3° with the current of 4.07 A, which is negligibly small.

As an experiment, a W-band sheet electron beam tube is manufactured and tested with the parameters given above. The initial sheet beam cross section is 10 mm×0.5 mm, and the cross section of the drift tube is 15 mm×1 mm. The testing magnetic field distribution is shown in Fig. 3. The experimental transmission rate is 100% when the beam voltages are 20 kV and 40 kV, the corresponding beam currents are 0.50 A and 1.49 A. The transmission rate reduces to 98.8% and 98.3% when the beam voltage increases 60 kV and 80 kV, respectively, and the beam currents are 2.78 A and 4.12 A, respectively. The amplitude of oscillation and the tilt angle increase due to the larger voltage, resulting in the falling of the transmission rate.

The envelopes and the tilt angles demonstrated in Fig. 4 are analysed in the tilted coordinate system, whereas the electron trajectory is analysed with the single-particle orbit theory in the laboratory coordinate system. In order to compare the results, we need to make a transformation of the envelopes in Fig. 4 from the tilted coordinate system to the laboratory coordinate system. Obviously, we have $a\,(z) = a\,(s)\cos[\theta\,(s)]$ and $b\,(z) = b\,(s)\cos[\theta\,(s)]$.

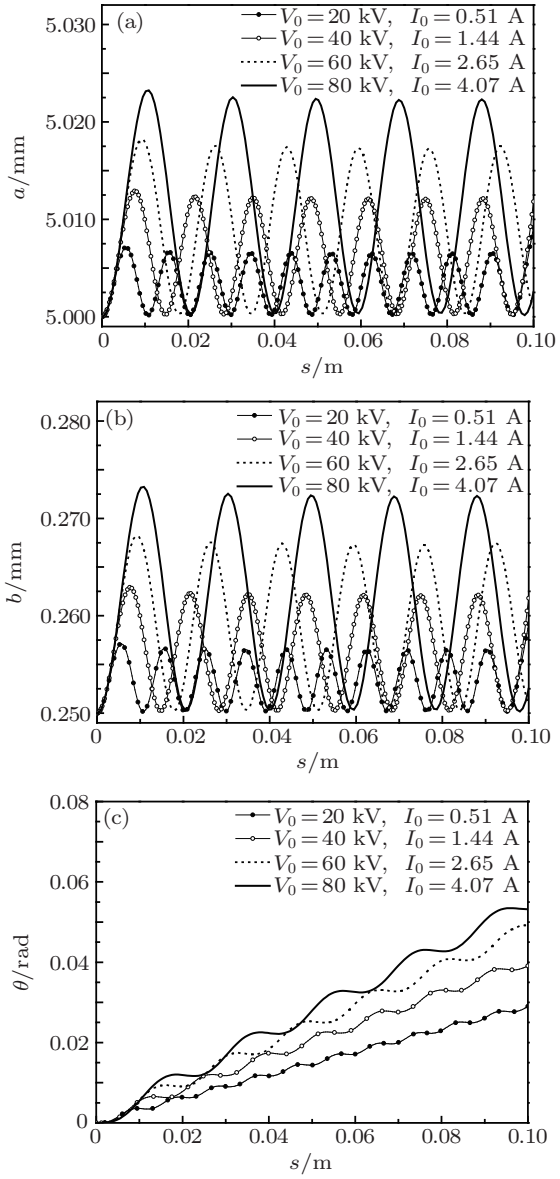


Fig. 4. Envelopes (a) $a\,(s)$, (b) $b\,(s)$, and tilted angle (c) $\theta\,(s)$ versus axial transport distance s for various voltages and currents.

Figure 5 shows the electron trajectories in the laboratory system at the edges of the beam in the xz and the yz planes. The beam voltage is $V_0 = 80$ kV,

and the current is $I_0 = 4.07$ A. The results from the single-particle orbit theory and the macroscopic cold-fluid model are compared. It is demonstrated that the oscillations of envelope $a(z)$ obtained from the two theories are almost identical, as shown in Fig. 5(a). The amplitude of oscillation obtained with the macroscopic cold-fluid model is smaller, owing to the larger space-charge field. Likewise, the trajectories of envelope $b(z)$ shown in Fig. 5(b) accord well with each other, while the amplitude of oscillation obtained with the macroscopic cold-fluid model is somewhat larger due to the smaller space-charge field, as have been expected in Section 3. The tilted angles normalized to their maximum values obtained from the two theories in the laboratory system are shown in Fig. 5(c),

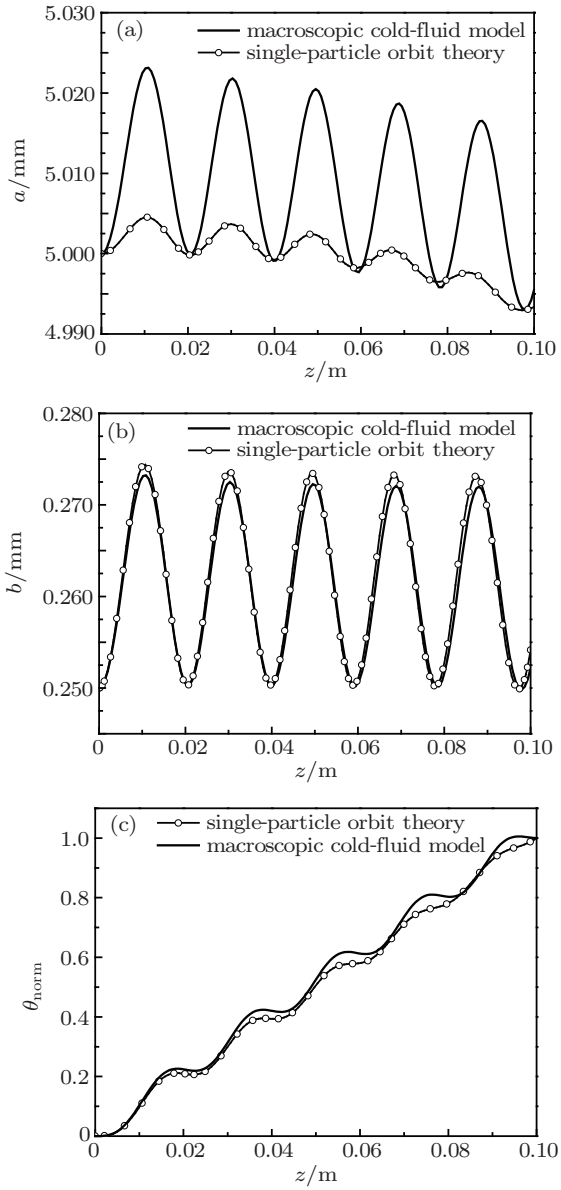


Fig. 5. Envelopes (a) $a(z)$, (b) $b(z)$, and normalized tilted angle (c) $\theta_{\rm norm}(z)$ versus axial transport distance z.

which demonstrates that the variations of the tilted angles from the two theories are approximately identical. Because the space-charge field in the x direction used in the single-particle orbit theory is much smaller than that used in the microscopic cold-fluid model, the tilted angle obtained in the former one is smaller than that in the latter one.

As shown in Fig. 5, the results obtained with the macroscopic cold-fluid model and the single-particle orbit theory are consistent with each other. When the space-charge fields are calculated numerically, the macroscopic cold-fluid model introduces an approximate formula in free space, while the single-particle orbit theory treats them in a rectangular drift tube. Hence, the single-particle orbit theory is more accurate than the macroscopic cold-fluid model. However, the macroscopic cold-fluid model describes the transport process clearly and is very helpful for understanding the characteristics of sheet beams.

5. Conclusion

The focusing and the stable transport of an intense elliptic sheet electron beam in a uniform magnetic field are investigated by using the macroscopic cold-fluid model and the single-particle orbit theory. The envelope equations are derived by making use of the macroscopic cold-fluid model, which provide detailed information about the beam dynamics, including the beam density, the velocity profile, and the tilt angle of the beam. The trajectories of the electrons projected at arbitrary initial positions can be numerical calculated by using the single-particle orbit theory. Comparing the envelopes and the tilted angles, we conclude that the results obtained from the two theories are consistent. The macroscopic cold-fluid model and the single-particle orbit theory presented in this paper are very effective to investigate the transport of a sheet beam. Furthermore, the macroscopic cold-fluid model is also the effective mean to study the instability of the sheet beam owing to its collective character.[12]

References

[1] Kyhl R L and Webster H F 1956 *IRE Trans. Electron Devices* **ED-3** 172
[2] Cutler C C 1956 *J. Appl. Phys.* **27** 1028

[3] Booske J H, McVey B D and Antonsen T M 1993 *J. Appl. Phys.* **73** 4140

[4] Booske J H, Basten M A, Kumbasar A H, Antonsen T M, Bidwell S W, Carmel Y, Destler W W, Granatstein V L and Radack D J 1994 *Phys. Plasmas* **1** 1714

[5] Burke A, Besong V, Granlund K, Jensen A J, Jongewaard E, Phillips R, Rauenbuehler K, Scheitrum G and Steele R 2006 *IEEE International Vacuum Electronics Conference*, April 25–27, 2006 Monterey, USA, p. 485

[6] Destler W W, Cheng S, Zhang Z X, Antonsen T M, Granatstein V L, Levush B and Rodgers J 1994 *Phys. Plasmas* **1** 1708

[7] Basten M A and Booske J H 1999 *J. Appl. Phys.* **85** 6313

[8] Nguyen K T, Pasour J A, Antonsen T M, Larsen P B, Petillo J J and Levush B 2009 *IEEE Trans. Electron Devices* **56** 744

[9] Zhao D 2009 *Phys. Plasmas* **16** 113102

[10] Jing Z, Bhatt R and Chen C P 2006 *Phys. Rev. Spec. Top. Accel. Beams* **9** 034404

[11] Jing Z, Bhatt R and Chen C P 2005 *Proc. 2005 Particle Accelerator Conference*, May 16–20, 2005 Knoxville, USA, p. 853

[12] Han Y and Ruan C J 2011 *Chin. Phys.* B **20** 104101